An Electret-Based Thermoacoustic-Electrostatic Power Generator

Geng Chen[1, 2], Lihua Tang[1,*], Zhaoshu Yang[1], Kai Tao[3], Zhibin Yu[2,*]

1. Department of Mechanical Engineering, University of Auckland, 20 Symonds Street, Auckland 1010, New Zealand

2. James Watt School of Engineering, University of Glasgow, Glasgow G12 8QQ, UK

3. School of Mechanical Engineering, Northwestern Polytechnical University, Xi'an, 710072, China

Correspondence: l.tang@auckland.ac.nz and Zhibin.Yu@glasgow.ac.uk

Summary

This study reports a new concept for power generation from thermal energy, which integrates a thermoacoustic engine (TAE) with a contact-free electret-based electrostatic transducer. The TAE converts thermal energy into high-intensity acoustic energy, while the electret-based electrostatic transducer converts the generated acoustic energy into electricity. The experiments demonstrate the feasibility and potential of the proposed electret-based thermoacoustic-electrostatic power generator (TAEPG). The dynamic response of the electrostatic transducer and energy conversion inside the TAE are further investigated using a lumped element model and a frequency-domain reduced-order network model. Good agreement is achieved between experimental measurements and theoretical predictions. Furthermore, a parametric study is performed to study the effect of key parameters including the external heating power, air gap and resistive load on the performance of the TAEPG. Results show that an open-circuit voltage amplitude of 4.7 V is produced at a closed-end pressure amplitude of 480 Pa in the experiment, and it is estimated that 25.2% of the acoustic power generated by the TAE has been extracted by the electret-based electrostatic transducer. In this case, the maximum electric power output is measured to be 2.91 μW at a resistive load of around 2.2 MΩ. By increasing the external heating power, the TAEEH can produce a maximum voltage amplitude of 8 V. This work shows that the proposed concept has great potential for developing miniature heat-driven power generators.

KEYWORDS

thermoacoustic engine, electrostatic transducer, electret, power generator, network model

1. INTRODUCTION

Thermoacoustic engines (TAEs) or prime movers attract great attention in the past decades because they can convert heat from various sources (low-grade industrial waste heat, solar energy, excess heat

in microelectronic systems, etc.) into acoustic oscillations with no moving parts.[1] The working principle behind the TAEs is the thermoacoustic effect which concerns mutual interaction between the acoustic and thermal fields around the solid-fluid interfaces.[2-8] The TAEs can be further transformed into electric power generators by acoustically coupling them with acoustic-to-electric transducers/converters, which provides novel alternative systems for power generation from low-grade thermal energy for niche applications.[9] So far, lots of efforts have been made towards the design and fabrication of robust acoustic-to-electric transducers for thermoacoustic power generators. Recently, a review of different methods to realize the conversion of thermoacoustic power into electricity was reported.[10] The most common acoustic-to-electric transducers applied in thermoacoustics are loudspeakers[11] or linear alternators[12-14] based on the electromagnetic effect, and piezoelectric converters[15-17] using stress-sensitive piezoelectric ceramics. Linear alternators normally have higher power outputs (up to kW), but they are bulky and prohibitively expensive. Conventional loudspeakers, although cheap to fabricate, are poor in performance and not reliable for long-time operation. As for piezoelectric converters, they operate well at high frequencies and are suitable for compact thermoacoustic engines. However, the power output associated with these transducers is generally small and highly affected by the working temperature. Other less-common thermoacoustic transducers include magnetohydrodynamic (MHD) generators[18], bi-directional turbines[19], triboelectric nanogenerator[20], etc. Nonetheless, there is insufficient experimental data to confirm the efficiency and robustness of these transducers. To summarize, each acoustic-to-electric conversion technology has its advantages and drawbacks and is therefore only suitable for some specific occasions. More work needs to be done to explore a promising alternative that possesses a better energy generation performance with fewer limitations.

In recent years, the electrostatic transductions have received considerable research interests as opposed to traditional piezoelectric and electromagnetic transductions for harvesting energy from various ambient energy sources.[21] Among them, electrostatic transducers using electrets (a dielectric material that has a quasi-permanent electric charge or dipole polarisation) are increasingly studied with the progress of MEMS technology and are believed to offer a viable solution to battery replacements for microelectronic devices such as autonomous wireless sensors.[22-26] Electret-based electrostatic transducers are variable-capacitor structures that use electrets with quasi-permanently implanted charges to generate electric current in response to a relative motion between the electrodes, thus directly convert vibrational energy into electricity. They possess four main advantages if utilized for thermoacoustic power generation. (a) It has a much simpler structure than other transducers such as electromagnetic devices, MHD generators, and bi-directional turbines. (b) The electret is contact-free from the counter electrode on a vibrating membrane, enabling it to withstand high temperatures and extract acoustic power reliably from the high-temperature regions of a TAE, proving more flexibility than all other transducers for coupling with TAEs. For instance, it effectively overcomes the temperature limitation faced by the piezoelectric or triboelectric transducers. (c) The cost of electrets is

normally lower than electromagnetic transducers or any piezoelectric ceramics. (d) Due to its simplicity, it is possible to build miniaturized, compact thermoacoustic power generators that operate at high frequencies.

In this study, we integrate an electret-based electrostatic transducer with a thermoacoustic engine, creating a new type of thermoacoustic power generator. The operating characteristics of the proposed electret-based thermoacoustic-electrostatic power generator are studied experimentally. Theoretical models are also established to investigate the key parameters that affect the performance of the thermoacoustic power generator. The rest of the paper is organized as follows. Section 2 introduces the experimental prototype and measurements. Section 3 describes the lumped element model and reduced-order network model for modelling the electrostatic transducer and thermoacoustic engine, respectively. Section 4 presents the experimental and theoretical results. Finally, concluding remarks are drawn in Section 5.

2. EXPERIMENTAL STUDY

Figure 1 illustrates the schematic diagram of an electret-based thermoacoustic power generator which comprises a standing-wave quarter-wavelength TAE and an electret-based electrostatic transducer working in out-of-plane mode.[21] The TAE is composed of a hot buffer, a resonator and a parallel-plate stack sandwiched between a hot heat exchanger (HE) and a cold heat exchanger. The transducer, placed at the left end of the hot buffer, consists of an electret layer on a base electrode and a counter electrode on a deformable membrane that is clamped at the rim. When thermoacoustic oscillations are initiated, the closed-end transducer will be driven by the self-sustained acoustic oscillations generated inside the TAE, which meanwhile radiates sound into the open ambient space at the right end of the resonator.
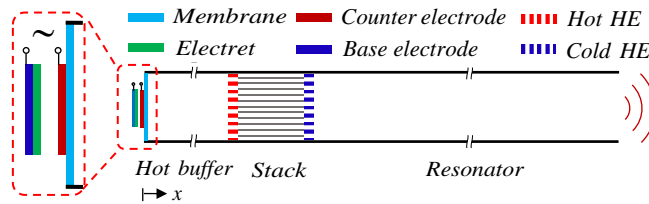

FIGURE. 1. Schematic of an electret-based standing-wave thermoacoustic-electrostatic power generator.

Figure 2A shows the prototype of an electret-based electrostatic transducer. The electret together with the base electrode is fixed by a support (black, 3-D printed) whose axial position can be adjusted through four bolts on its outer edges. The transducer can be represented by an equivalent circuit model[27] in Figure 2B, where Q_1 and Q_2 are positive charges on the base and counter electrodes, C_{eq} represents the equivalent series capacitance of the electret and air gap, V_S denotes the surface potential of the electret induced by the negative charges Q_E (constant in amount) implanted in the electret, R_L is the resistive

3

load and C_p stands for the parasitic capacitance. According to the Gauss's law, Q_E in the electret (Figure 2C) is equal to the sum of the positive charges Q_1 and Q_2. As the transducer is subject to pressure oscillations inside the TAE, the real-time distance $d_1 = d_0 + w_{r1,m}\sin(\omega t)$ between the electret and counter electrode (d_0 is the initial air gap, $w_{r1,m}$ is the mean displacement of the counter electrode and ω is the angular frequency) leads to a change in C_{eq} and charge migration between the base and counter electrodes. Figure 2D displays four representative instants in an acoustic cycle when the counter electrode is at its left-most, neutral and right-most positions. At the left-most position, Q_1 is minimum while Q_2 is maximum. As the counter electrode moves to the right, positive charges on the counter electrode flow to the base electrode until the counter electrode reaches the right-most position where Q_2 is minimum and Q_1 is maximum. Then, the counter electrode moves leftwards, transferring positive charges on the base electrode to the counter electrode. As a result, an alternating current I (leading the displacement by a phase of $\pi/2$) through R_L is generated and part of the mechanical energy is converted into electricity.
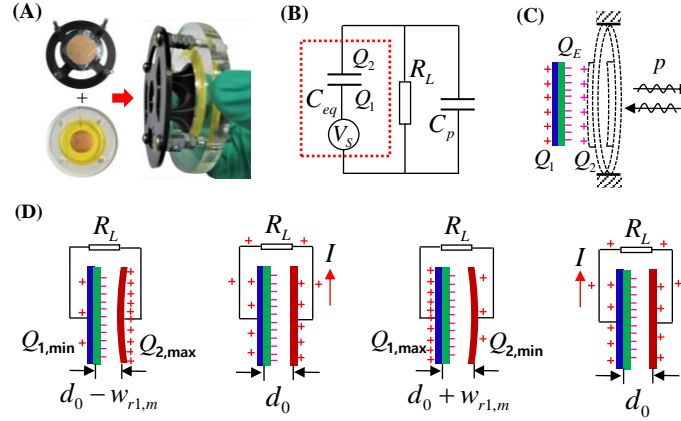

FIGURE. 2. Working principle of the electret-based electrostatic transducer. A, prototype of the transducer; B, equivalent circuit representation of the electret-based electrostatic transducer; C, deformation of the membrane under pressure oscillations; D, four representative moments in an acoustic cycle.

Table 1 lists the dimensions of the TAE and characteristic parameters of the electrostatic transducer in the experiment. The stack, electrodes and membrane are made of alumina ceramic (Al_2O_3), copper (Cu) and polyethylene terephthalate (PET) plastic, respectively. For simplicity, we omitted the cold heat exchanger and used a nichrome resistance wire (connected to an adjustable power supply) to serve as the hot heat exchanger[15]. Detailed information of the TAE rig can be found in Ref.15. In terms of the measurements, the temperatures at the stack ends are measured using two thermocouples (National Instruments, J and K-types). Two microphones (3M Quest Technologies, QE 4110; GRAS, 40PH) are placed at the left end of hot buffer and right end of resonator to monitor the closed-end and open-end pressure oscillations. The instantaneous voltage across the resistive load is measured via a data acquisition module (National Instruments, NI9205).

4

TABLE 1. Parameters of the TAE and electret-based electrostatic transducer.

TAE	Values
Tube diameter D	0.05 m
Hot buffer length L_H	0.1 m
Stack length L_S	0.04 m
Resonator length L_R	0.36 m
Stack plate thickness t_S	1×10^{-3} m
Stack plate gap d_S	1×10^{-3} m
Transducer	**Values**
Electrode radius r_1	0.015 m
Electrode thickness h_1	1×10^{-4} m
Electrode density ρ_1	8,960 kg / m³
Membrane radius r_2	0.025 m
Membrane thickness h_2	3×10^{-4} m
Membrane density ρ_2	1,400 kg / m³
Electret radius r_3	0.015 m
Electret thickness h_3	1×10^{-4} m
Dielectric coefficient of vacuum ε_0	8.85×10^{-12}
Relative dielectric coefficient ε_1	2
Surface potential V_S	1900 V
Parasitic capacitance C_p	78 pF

3. THEORETICAL MODELLING

3.1 Electrostatic transducer

Following the experiment, a lumped element model (LEM) is utilized here to predict the dynamic behaviour of the electrostatic transducer. It is assumed in LEM that the dynamic responses of displacements approximate those under static conditions. Thus, the short-circuit deflections w_{r1} for the two-layer segment (with radius r_1) and w_{r2} for the one-layer segment (with inner radius r_1 and outer radius r_2) under a uniform predefined static pressure load p_{load} can be calculated, the derivation process of which is described in Ref. 15. Then, assuming a time-harmonic motion $w_{r1}\sin(\omega t)$, the equivalent dynamic series capacitance C_{eq} of the electret and air gap is written as

$$C_{eq} = \int_0^{r_1} \frac{2\pi r \varepsilon_0}{h_3 / \varepsilon_1 + d_0 + w_{r1}\sin(\omega t)} dr \tag{1}$$

where r is the radial coordinate, ε_0 is the dielectric coefficient of vacuum, ε_1 is the relative dielectric coefficient and h_3 is the electret thickness. Assuming the amount of charges transferred between the base and counter electrodes is Q, according to the Kirchhoff's law, the governing equation for the electret-based electrostatic transducer (Figure 2B) is written as,[27]

$$\frac{dQ}{dt} = \frac{C_{eq}}{C_{eq} + C_p}\left(\frac{V_s}{R_L} - Q\left(\frac{1}{R_L C_{eq}} - \frac{C_p}{C_{eq}^2}\frac{dC_{eq}}{dt}\right)\right) \tag{2}$$

which can be solved using a classical Runge-Kutta method.[28] Finally, the instantaneous voltage V_L across the resistive load R_L is

$$V_L = V_s - Q / C_{eq} \tag{3}$$

and the corresponding time-averaged power output P can be approximated by

$$P = V_A^2 / \left(2R_L\right) \tag{4}$$

where V_A is the amplitude of the alternating voltage.

3.2 Thermoacoustic engine

For the modelling of TAE, a frequency-domain, reduced-order network model is adopted to describe the energy conversion process inside the TAE. The TAE, together with a predefined axial temperature distribution, is firstly evenly discretized into a large number of sub-segments with each sub-segment satisfying the linearized quasi-one-dimensional continuity and momentum conservation equations in the thermoacoustic theory,[2]

$$\frac{dU_1}{dx} = -\left(1 + (\gamma - 1)f_k\right)\frac{j\omega A}{\gamma p_m}p_1 + \frac{f_k - f_v}{(1-\sigma)(1-f_v)}\frac{1}{T_m}\frac{dT_m}{dx}U_1 \tag{5}$$

$$\frac{dp_1}{dx} = -\frac{j\omega\rho_m}{A(1-f_v)}U_1 \tag{6}$$

where the subscripts "m" and "1" represent the mean and first-order harmonic fluctuation values, respectively. j is the imaginary unit of complex numbers. T and ρ are the static temperature and density of the working fluid. U_1 is the volume velocity (product of cross-sectional area A and velocity u_1). γ is the specific heat ratio an σ is the Prandtl number. f_v and f_k are thermo-viscous functions determined by the geometry and dimensions of the flow channels.[29] Continuity of acoustic pressure p_1 and volume velocity U_1 are assumed at the interfaces between two adjacent sub-segments.

For the boundary conditions at the TAE ends, impedance matching gives

$$\begin{cases} Z_0 = -Z_T = -A^2\left(j\omega M_{eff} - jK_{eff}/\omega + C_{eff}\right) \\ Z_L = Z_R = 0.6 j\omega\rho_m r_2 / A + 0.25\rho_m\left(r_2\omega\right)^2 / \left(cA\right) \end{cases} \tag{7}$$

where c is the speed of sound; Z_0 and Z_L are acoustic impedance of the working fluid at the left and right ends, respectively; Z_T and Z_R are the equivalent acoustic impedance of the closed-end electrostatic transducer and open-end sound radiation. Z_0 and Z_T have opposite signs because a positive pressure

inside the working fluid leads to a negative velocity of the transducer. The acoustic radiation impedance Z_R is approximated by a plane circular piston model for an unflanged (flange size is small with respect to the wavelength of sound) open-ended pipe.[30]

Note that, for the electrostatic transducer, the electrical components are omitted in Z_T since the electrical domain has negligible influence on the mechanical counterpart.[31] The effective mass M_{eff}, stiffness K_{eff}, and damping coefficient C_{eff} of the electrostatic transducer are calculated by

$$\begin{cases} M_{eff} = \left(\int_0^{r_1} w_{r1}^2 \left(\rho_1 h_1 + \rho_2 h_2 \right) 2\pi r dr + \int_{r_1}^{r_2} w_{r2}^2 \rho_2 h_2 2\pi r dr \right) / w_m^2 \\ K_{eff} = p_{load} A / w_m, \quad C_{eff} = 2\xi \sqrt{M_{eff} K_{eff}} \end{cases} \tag{8}$$

where the damping ratio ξ is assumed to be 0.018 in this study.[17] ρ_1, h_1 and ρ_2, h_2 are densities and thicknesses of the counter electrode and membrane, respectively. The expressions for the short-circuit deflections w_{r1} and w_{r2} under uniform static pressure load p_{load} can be found in Ref. 15. w_m is the mean displacement of the counter electrode together with the membrane, i.e.,

$$w_m = \left(\int_0^{r_1} w_{r1} 2\pi r dr + \int_{r_1}^{r_2} w_{r2} 2\pi r dr \right) / A \tag{9}$$

Finally, based on the transfer matrix method,[15] the impedance boundaries Z_0 and Z_L at the TAE ends in Equation (7) can be related by a total transfer matrix (product of matrices of all sub-segments). Thereby, a characteristic (frequency) equation is created, the solution of which is the eigenfrequencies of the entire thermoacoustic power generator. Then, the eigenvectors (axial distributions of p_1 and U_1) are obtained by integrating Equations (5) and (6) along the TAE. The time-averaged acoustic power at each position x can be calculated by[2]

$$W = \Re[p_1 \tilde{U}_1] / 2 \tag{10}$$

where $\Re[\ ]$ denotes the real part of a complex quantity and the tilde " $\tilde{}$ " stands for the complex conjugate.

4. RESULTS AND DISCUSSIONS

4.1 Dynamic response

Following the theoretical analyses of the transducer and TAE, the instantaneous closed-end acoustic pressure $p(0)$, open-end acoustic pressure $p(L)$ and open-circuit ($R_L = 10$ GΩ) voltage V_L were first measured at a heating power Q_{in} of 106 W when the temperatures at the stack ends asymptote at 540 K and 420 K after the stack was heated for around 30 minutes. The data were recorded when we swiftly removed the piece of paper that blocked the open end to prohibit thermoacoustic instability.

As seen from Figure 3, spontaneous acoustic oscillations occur shortly after the blockage is removed. Then, the TAE reaches a steady state (limit cycles) after a short saturation process. The steady-state pressure waveforms and corresponding Fast Fourier Transform (FFT) analyses in Figures 3A and 3B indicate that the acoustic pressure waves are nearly harmonic inside the TAE, oscillating at the frequency of 166.1 Hz. This frequency is very close to the fundamental eigenfrequency of 165.7 Hz predicted by the network model after substituting the measured temperature distribution into Equations (5) to (7). The open-end pressure amplitude is significantly smaller than that in the closed end. For the open-circuit voltage from the transducer in Figure 3C, evident distortions in the waveform are observed, which can be verified through the spectrum analysis where the second harmonic (332.1 Hz) arises. The harmonic distortions appear because the voltage output is not linearly proportional to the displacement of the counter electrode as inferred from Equation (1) where $w_{r1}\sin(\omega t)$ is one part of the denominator. However, if the displacement amplitude is small, the waveforms will become quasi-sinusoidal. Currently, the prototype produces an open-circuit voltage of 4.7 V at a closed-end pressure amplitude of 480 Pa. Substituting the measured pressure amplitude p_A (480 Pa in replacement of p_{load}), oscillation frequency f (166.1 Hz) and initial air gap d_0 (1 mm) into Equations (1) to (3), yields the analytical results of open-circuit voltage V_L (dotted curve). Note that, the amplitude of the mean displacement $w_{r1,m}$ of the counter electrode is calculated to be around 0.2 mm in this case. Good agreement between the experimental measurements and theoretical predictions with regard to V_L is achieved as shown in Figure 3C. The small deviation might be attributed to intrinsic nonlinearity in the electrostatic transducer that results in a larger proportion of second harmonic in the experiment.
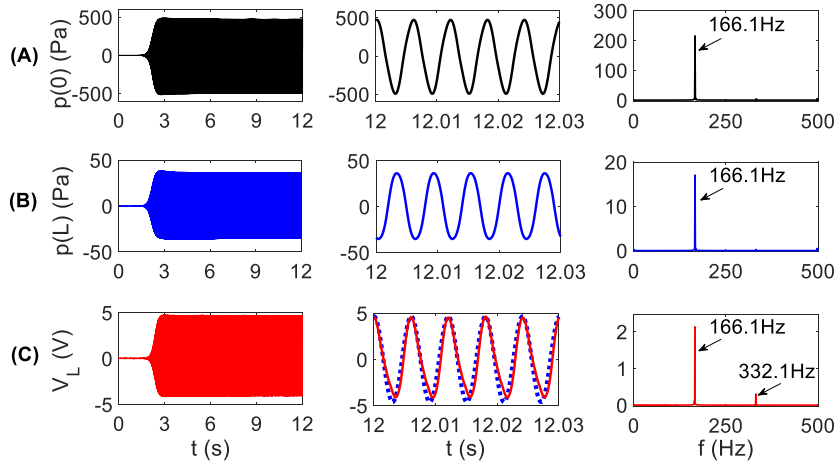

FIGURE. 3. A, time-series and FFT analyses of closed-end acoustic pressure $p(0)$; B, time-series and FFT analyses of open-end acoustic pressure $p(L)$; C, time-series and FFT analyses of open-circuit alternating voltage V_L in the experiment. The dotted curve represents theoretical predictions.

4.2 Acoustic field

Figure 4 plots the longitudinal distributions of the magnitudes of acoustic pressure $|p_1|$, axial velocity magnitude $|u_1|$, acoustic impedance $|Z| = |p_1 / (u_1 A)|$ and time-averaged acoustic power W. The shaded

area indicates where the stack is located. It should be mentioned that the acoustic field is obtained after we integrate the Equations (5) to (6) along the TAE using the measured closed-end ($x = 0$ m) pressure amplitude (480 Pa) and oscillation frequency (166.1 Hz). The open-end ($x = 0.5$ m) pressure amplitude calculated (35.2 Pa) in Figure 4A matches well with that measured (35.5 Pa) in Figure 3B, which verifies the network model used in this study. For the standing-wave quarter-wavelength TAE, the pressure antinode exists at the closed end whereas velocity antinode is located at the open end. Thus, the acoustic impedance is maximum at the closed end and decreases gradually towards the open end. In Figure 4D, an increase of acoustic power $\Delta W = W_R - W_L$ (W_R and W_L are acoustic power at the right and left ends of the stack) is observed in the stack region. It is found that most of acoustic power generated is dissipated by the irreversible viscous and thermal-relaxation losses inside the hot buffer and resonator as well as the open-end acoustic radiation, while only a small proportion of the power gain is extracted by the closed-end transducer. In this case, the corresponding acoustic power extraction rate $\eta_1 = |W(0)|/\Delta W$ is calculated to be 0.252 with $W(0)$ being the acoustic power at the closed end.
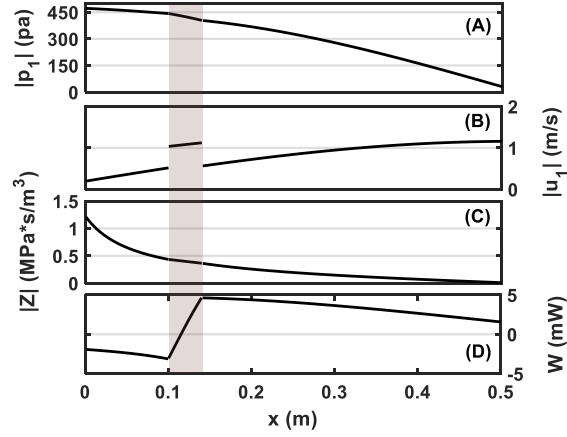

FIGURE. 4. Longitudinal distributions of A, the magnitude of acoustic pressure $|p_1|$; B, the magnitude of axial velocity $|u_1|$; C, the magnitude of acoustic impedance $|Z|$; D, time-averaged acoustic power W.

4.3 Parametric study

Figure 5 shows the effects of external heating power Q_{in}, initial air gap d_0 and resistive load R_L on the performance of the thermoacoustic power generator. The discrete points are the experimental measurements while dashed curves are from theoretical calculations.

It is found in Figure 5A that the steady-state pressure amplitude p_A measured at the closed end, open-circuit voltage amplitude V_A and oscillation frequency f increase with the increase of Q_{in}. A maximum voltage amplitude of 8 V is observed, corresponding to a pressure amplitude of 744 Pa. Note that, theoretical predictions of limit-cycle pressure amplitudes are unavailable at this stage due to lack of a reliable time-domain, nonlinear network model that considers nonlinear viscous and thermal losses at large amplitudes.[9] However, the open-circuit voltage and oscillation frequency can be estimated from the lumped element model and frequency-domain, reduced-order network model. Close match is

9

obtained between the theoretical estimates and experimental measurements. Difference between measured and assumed axial temperature distributions might account for the minor deviations.[15]

In Figure 5B, when the heating power is kept constant (Q_{in} = 106 W), the increase of air gap d_0 has negligible effects on p_A and f and is thereby not displayed. However, it has a significant effect on V_A through series capacitance C_{eq}, as confirmed by the decreasing trend of V_A measured in the experiment. It can be also seen from Figure 5B that, the measured V_A is consistent with the theoretical predictions as d_0 increases.

In Figure 5C, where Q_{in} =106 W and d_0 = 1 mm, the time-averaged power output is measured to peak at 2.91 µW at a resistive load of around 2.2 MΩ. However, an optimal time-averaged power output P_{opt} of 3.41 µW is predicted at the optimal resistive load R_{opt} of 2.01 MΩ. In this case, the acoustic-to-electric efficiency $\eta_2 = P_{opt}/|W(0)|$ is estimated to peak at 0.18%. The measured power output peak is 14.6 % smaller than the theoretical counterpart. The discrepancy occurs partly because of systematic errors arising from either approximation of power output using Equation (4), or measurement/calibration inaccuracies of the data acquisition systems for measuring V_A and R_L. Another possible reason for the discrepancy is because a few charges injected into the electret are lost due to long-time operation or change of environmental conditions.[27]
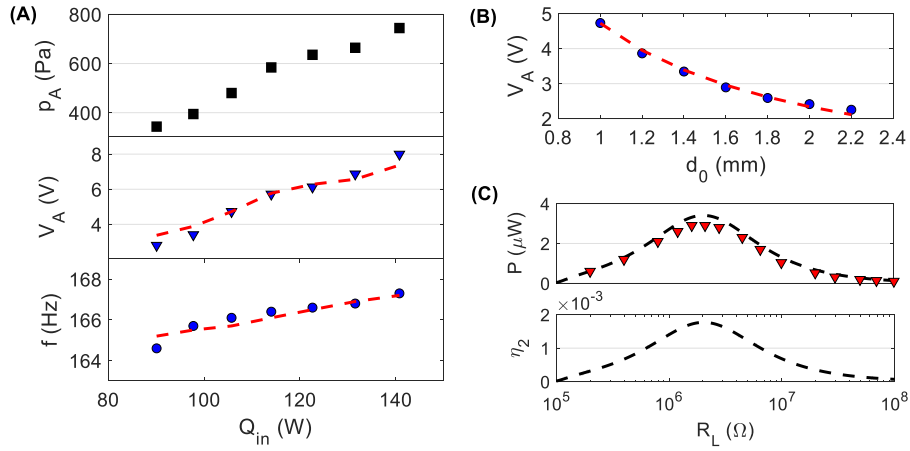

FIGURE. 5. A, effect of external heating power Q_{in} on the steady-state pressure amplitude p_A, open-circuit voltage amplitude V_A and oscillation frequency f; B, effect of initial air gap d_0 on the open-circuit voltage amplitude V_A; C, effect of resistance R_L on the electric power output P and acoustic-to-electric efficiency η_2. The discrete points are the experimental measurements while dashed curves are from theoretical calculations.

4.4 Future optimization

Owing to the simplicity of both the TAE and electret-based transducer, the proposed concept has great potential for developing miniature heat-driven power generators to provide power for microelectronic

devices such as microcontrollers, sensors, chips, etc, which usually require ultra-low power consumptions.

It is worth noting that the simple prototype built in this study is primarily used to prove the above concept. It adopts an open TAE using atmospheric air as working fluid, and thus only produces very little power. However, the power output of the proposed thermoacoustic power generator can be significantly improved to usable levels if the TAE and electrostatic transducer are carefully optimized in the future. For the TAE, it is possible to implement more efficient travelling-wave TAEs with pressurized helium as working gas, which have achieved thermal efficiencies comparable to conventional engines[32]. The travelling-wave TAEs also own lower onset temperatures and therefore have a wider temperature range for proper operation. For the electrostatic transducer, efforts could be made towards reducing the value of parasitic capacitance which has a great effect on the output voltage.[27] It is also plausible to enhance the transducer performance by increasing the electret surface potential or adapting the capacitor shapes, etc.[27]

5. CONCLUSIONS

We have proposed a new device for power generation, namely, an electret-based thermoacoustic-electrostatic power generator that is capable of converting heat energy into electricity, and a prototype is built to demonstrate the concept. The dynamic responses of the electrostatic transducer and standing-wave thermoacoustic engine are investigated experimentally and compared with the theoretical models. Good agreement is achieved between the experimental measurements and theoretical predictions, which verifies the lumped element model for the electrostatic transducer and reduced-order network model for the thermoacoustic engine in this study. Besides, the effect of key parameters on the system performance is examined through a series of experimental and theoretical studies, which gives deeper insight into the characteristics of the thermoacoustic power generator. Experimental results show that the power generator is able to produce a maximum voltage amplitude of 8 V when the external heat input increases. The voltage output decreases gradually as the initial air gap increases. A peak power output of 2.91 μW is observed at a resistive load of around 2.2 MΩ. Although not efficient at present, the new thermoacoustic power generator demonstrated in this paper has great potential for developing miniature power sources for microelectromechanical systems by utilizing low-grade thermal energy.

ACKNOWLEDGEMENTS

REFERENCES

1.   Rott N. Thermoacoustics. *Advances in applied mechanics* 1980, 20:135-175.

2.   Swift GW. *Thermoacoustics: A unifying perspective for some engines and refrigerators*: Springer; 2017.

3.   Li DH, Zhang LM, Wu ZH, Luo EC. Numerical simulation and experimental investigation of a gas‐liquid, double‐acting traveling‐wave thermoacoustic heat engine. *International Journal of Energy Research* 2013, 37:1963-1970.

4.   Dhuchakallaya I, Saechan P. Design and experimental evaluation of a travelling‐wave thermoacoustic refrigerator driven by a cascade thermoacoustic engine. *International Journal of Energy Research* 2017.

5.   Yang R, Wang Y, Jin T, Feng Y, Tang K. Performance optimization of the regenerator of a looped thermoacoustic engine powered by low‐grade heat. *International Journal of Energy Research* 2018, 42:4470-4480.

6.   Hao H, Scalo C, Sen M, Semperlotti F. Thermoacoustics of solids: A pathway to solid state engines and refrigerators. *Journal of Applied Physics* 2018, 123:024903.

7.   Chen G, Tang L, Mace BR. Theoretical and experimental investigation of the dynamic behaviour of a standing-wave thermoacoustic engine with various boundary conditions. *International Journal of Heat and Mass Transfer* 2018, 123:367-381.

8.   Chen G, Krishan G, Yang Y, Tang L, Mace B. Numerical investigation of synthetic jets driven by thermoacoustic standing waves. *International Journal of Heat and Mass Transfer* 2020, 146:118859.

9.   Swift GW. Thermoacoustic engines. *The Journal of the Acoustical Society of America* 1988, 84:1145-1180.

10.   Timmer MA, de Blok K, van der Meer TH. Review on the conversion of thermoacoustic power into electricity. *The Journal of the Acoustical Society of America* 2018, 143:841-857.

11.   Kang H, Cheng P, Yu Z, Zheng H. A two-stage traveling-wave thermoacoustic electric generator with loudspeakers as alternators. *Applied Energy* 2015, 137:9-17.

12.   Hamood A, Jaworski AJ, Mao X, Simpson K. Design and construction of a two-stage thermoacoustic electricity generator with push-pull linear alternator. *Energy* 2018, 144:61-72.

13.   Wang K, Sun D, Zhang J, Xu Y, Zou J, Wu K, Qiu L, Huang Z. Operating characteristics and performance improvements of a 500W traveling-wave thermoacoustic electric generator. *Applied Energy* 2015, 160:853-862.

14.   Yu Z, Jaworski AJ, Backhaus S. Travelling-wave thermoacoustic electricity generator using an ultra-compliant alternator for utilization of low-grade thermal energy. *Applied Energy* 2012, 99:135-145.

15.   Chen G, Tang L, Mace BR. Modelling and analysis of a thermoacoustic-piezoelectric energy harvester. *Applied Thermal Engineering* 2019, 150:532-544.

16.   Smoker J, Nouh M, Aldraihem O, Baz A. Energy harvesting from a standing wave thermoacoustic-piezoelectric resonator. *Journal of Applied Physics* 2012, 111:104901.

17.   Jensen C, Raspet R. Thermoacoustic power conversion using a piezoelectric transducer a. *The Journal of the Acoustical Society of America* 2010, 128:98-103.

18.   Castrejón-Pita A, Huelsz G. Heat-to-electricity thermoacoustic-magnetohydrodynamic conversion. *Applied physics letters* 2007, 90:174110.

19.   Badhurshah R, Dudhgaonkar P, Jalihal P, Samad A. High efficiency design of an impulse turbine used in oscillating water column to harvest wave energy. *Renewable Energy* 2018, 121:344-354.

20.   Zhu S, Yu A, Yu G, Liu Y, Zhai J, Dai W, Luo E. Thermoacoustically driven triboelectric nanogenerator: Combining thermoacoustics and nanoscience. *Applied Physics Letters* 2017, 111:153901.

21.   Wei C, Jing X. A comprehensive review on vibration energy harvesting: Modelling and realization. *Renewable and Sustainable Energy Reviews* 2017, 74:1-18.

22.   Yang Z, Tang L, Tao K, Aw K. A broadband electret-based vibrational energy harvester using soft magneto-sensitive elastomer with asymmetrical frequency response profile. *Smart Materials and Structures* 2019, 28:10LT02.

23.   Yang Z, Tang L, Tao K, Aw KC. Modelling and Validation of Electret-Based Vibration Energy Harvesters in View of Charge Migration. *International Journal of Precision Engineering and Manufacturing-Green Technology* 2019:1-11.

24.   Ahmed S, Kakkar V. An electret-based angular electrostatic energy harvester for battery-less cardiac and neural implants. *IEEE Access* 2017, 5:19631-19643.

25.   Hillenbrand J, Pondrom P, Sessler G. Electret transducer for vibration-based energy harvesting. *Applied Physics Letters* 2015, 106:183902.

26.   Perez M, Boisseau S, Gasnier P, Willemin J, Reboud J. An electret-based aeroelastic flutter energy harvester. *Smart materials and structures* 2015, 24:035004.

27.   Boisseau S, Despesse G, Ricart T, Defay E, Sylvestre A. Cantilever-based electret energy harvesters. *Smart Materials and Structures* 2011, 20:105013.

28.   Butcher JC. The numerical analysis of ordinary differential equations: Runge-Kutta and general linear methods. 1987.

29.   Arnott WP, Bass HE, Raspet R. General formulation of thermoacoustics for stacks having arbitrarily shaped pore cross sections. *The Journal of the Acoustical Society of America* 1991, 90:3228-3237.

30.   Kinsler LE, Frey AR, Coppens AB, Sanders JV. Fundamentals of acoustics. *Fundamentals of Acoustics, 4th Edition, by Lawrence E. Kinsler, Austin R. Frey, Alan B. Coppens, James V. Sanders, pp. 560. ISBN 0-471-84789-5. Wiley-VCH, December 1999.* 1999:560.

31.   Tao K, Wu J, Tang L, Hu L, Lye SW, Miao J. Enhanced electrostatic vibrational energy harvesting using integrated opposite-charged electrets. *Journal of Micromechanics and Microengineering* 2017, 27:044002.

32.   Backhaus S, Swift G. A thermoacoustic Stirling heat engine. *Nature* 1999, 399:335-338.